Received: 6 October 2022 | Accepted: 28 November 2022

DOI: 10.1002/pamm.202200101

Investigation of a Realistic Flap Modeling Using a Combination of Chimera Method and Grid Deformation on a Wing Fuselage Configuration

Marco Hillebrand[1,*], **Jens Müller**[1], **Junaid Ullah**[1], and **Thorsten Lutz**[1]

[1] University of Stuttgart, Faculty 6: Aerospace Engineering and Geodesy, Institute of Aerodynamics and Gas Dynamics, Pfaffenwaldring 21, 70569 Stuttgart, Germany

Flap deflections of an aircraft wing for active load alleviation within CFD simulations are realized using pure grid deformation due to time saving and low modeling complexity. In this case, spanwise gaps are neglected, which are present in reality during a flap deflection. Another possibility to realize the deflections is the combination of pure grid deformation and Chimera method, which allows the modeling of the gap between flap and wing or consecutive flaps. The overall aim of this work is the analysis of the aerodynamic effects caused by the different modeling approaches realizing leading and trailing edge flap deflections. The comparison of the modeling methods is investigated on the DLR LEISA configuration, which is a generic wing-fuselage configuration. For active gust load alleviation, the leading edge flaps are deflected downward and the trailing edge flaps are deflected upward. Due to the downward deflection of the leading edge flaps, vortices are formed using the combined Chimera method as a result of the gap consideration. These vortices lead to a local drag increase resulting in a difference between both modeling methods in the spanwise as well as global drag coefficient. With the pure grid deformation these vortices do not occur. Due to the upward trailing edge deflection, the combined Chimera method leads to a pressure compensation via the effective gap enlargement, which is not present in the pure grid deformation. Overall, the combined Chimera method offers a good possibility to model the induced drag as well as the pressure compensation at a large flap deflection.

1 Introduction

A major goal of the aircraft design process derives from Flightpath 2050, aiming for a 75% reduction in CO_2 emissions per passenger kilometer by 2050 [1]. In this context, a part is achieved via mass savings making aircraft structures increasingly elastic [2]. These structures are required to be certified in aircraft design in accordance with CS-25 [3]. An important part of the certification process is the consideration of gust loads, which are mainly responsible for the dimension of the structure and thus the mass [4]. In order to reduce the resulting gust loads on the wing, having a positive effect on the structural mass and thus on the aircraft mass, two options exist for load reduction with regard to passive and active gust load reduction. Within the Smart Fixed Wing Aircraft (SFWA), different methods were investigated for the two gust load alleviation approaches [5]. The passive gust load alleviation approach is based on a structural modification. For example, the aeroelastic wing behavior is adjusted by direction dependent stiffness properties of composite materials [5]. A disadvantage is mass increases due to stiffeners [6]. Whereas, active gust load systems based on the deflections of the existing control surfaces of the wing. This offers the possibility of static load re-distributions as well as dynamically actuated control surfaces, allowing a reduction of the critical loads during gust interaction and enabling lighter built wing [7]. First investigations on the application of dynamically actuated control surfaces for the reduction of maneuvering and gust loads were accomplished in [4], [5] and [8]. Here, the theory of dynamically actuated control surfaces is investigated in the context of an intelligent wing. Thereby, load fluctuations caused by gusts or turbulence shall be fully compensated, resulting in a "1g" wing. For this purpose a new system is investigated in the LuFo VI-3 project PoLamin, using deflections of segmented leading edge as well as trailing edge flaps (TEF) in cruise flight for gust load alleviation on a rigid aircraft. For transonic flight, only dynamic trailing edge flaps as well as aileron deflections have been investigated for gust load alleviation so far, as for example in [8], [9] and [10]. Thus, the combination of leading and trailing edge flaps is a special characteristic of PoLamin and the work at hand. The leading edge flaps (LEF) are used for torsional control and the trailing edge flaps for lift and bending moment control. Within the numerical investigations of gust alleviation, pure grid deformation is applied for the dynamic flap deflections due to the simple and fast application for the realization of the deflections. However, the gaps between control surface and wing in flow as well as in spanwise direction are neglected. Thus, flap deflections are represented in a simplified way. The pure Chimera method can be used to take both gaps, in spanwise and flow direction, into account. However, this is very costly, time consuming, and complex in terms of mesh generation. A compromise represents the combination of Chimera method and pure grid deformation [11]. Here, only the the spanwise gap is modeled. The gap in flow direction, normally covered by the spoiler, is shown as closed via pure grid deformation. A comparison between pure grid deformation as well as the combination of Chimera modeling and pure grid deformation on the LANN wing can be found in [11], [12]. Another possibility of modeling is offered by the sliding interfaces described in [12]. The primary aim of the current investigation is the analysis of the spanwise gap influence in the

* Corresponding author: e-mail marco.hillebrand@iag.uni-stuttgart.de, phone +49 711 685 63409

modeling of flap deflections in transonic flow. Thereby, aerodynamic deviations due to the different modeling respectively the influence of neglecting the spanwise gaps on the aerodynamics are evaluated. These findings are used to assess whether the modeling of the flap deflections by means of the pure grid deformation is sufficient or whether the consideration of the spanwise gaps is elementary important. The studies will be performed on the generic wing fuselage DLR LEISA configuration used in [13] and [14].

2 Numerical Setup

The control surface layout of the DLR LEISA configuration is derived from the multifunctional control surfaces of the Pro-HMS project [15] and transferred to the DLR LEISA configuration in the work of Ullah et al. [13], [14]. Furthermore, the underlying baseline computational grid, used in this work, is described in [13]. It is a hybrid unstructured grid consisting of an unstructured surface and volume grid and a prismatic grid representing the boundary layer. This Baseline grid is refined for the present work in the wing near field, on the wing surface at the TEF and LEF regions and in the region of the wing fuselage junction. Due to the refinement, the grid contains 146 mio points. The refined surface grid of the DLR LEISA configuration is shown black in Figure 1, which includes the complete wing and the control surfaces. The reason for refinement is to achieve a sufficiently good interpolation using the combined Chimera method.To obtain comparability between the two types of flap modeling, the refined grid is used for both modeling methods. For the combined Chimera method the refined grid is used as background grid. The flap grids are subsequently added to this using the Chimera method. The setup of the flap grids based on the combined Chimera method is described in [11], [12] and is presented in the following for the DLR LEISA configuration. If a single flap is modeled, the grid consists of three parts. Two grids create the transition to the right and left of the wing. These grids will be named cover grids in the following and are marked red in Figure 1. The third grid contains the control surface and is located between the two cover grids. It is connected to the two lateral cover grids by the Chimera method. Thus, an interpolation area exists between the control surface and cover grid to the background grid as well as between the cover and control surface grids. The gap between cover grid and control surface grid is generated with 10 elements of equal width and the interpolation region in the gap includes 6 elements. Additionally, the grids overlap in the interpolation region. Furthermore, a hole is cut in the baseline grid to blank it. The gap width is based on [12] and corresponds to $0.1\%c_{root}$. If several flaps are modeled next to each other, the cover grids are located only at the outer positions. At the DLR LEISA configuration, this corresponds once to the wing tip and once to the wing root. For a more detailed view, the cover grids are shown red in Figure 1. Furthermore, the Chimera boundary and the control surface grids are visible in the detailed view in blue. The latter also demonstrates the transition between the individual flaps respectively the interpolation region between the flaps via the flap grids. In addition, Figure 1 shows the structured realization of the control surface and cover grids. The resulting grid for the combined Chimera method has 979 orphan points distributed in the flow field without flap deflection. In total, the grid with the Chimera control surfaces included, is constituted by 270 mio points. Thus, the orphan points constitute 0.0004% of the total grid points. In combination with the fact that the orphan points do not occur in one place and not directly on the wing surface, this grid can be used for simulations. For the flap deflection analyzed in Section 4, the number of orphan points increases to 14.284. The transonic flow condition considered is given by a Reynolds number of $6.4e^6$ at a Mach number of $M = 0.8$ and an angle of attack of $\alpha = 0.957°$. For comparability, the numerical setup is almost identical for both modeling types. Therefore, the Spalart-Allmaras turbulence model is applied in its negative form and scalar dissipation is utilized as central dissipation scheme. Due to numerical instabilities skew symmetric kok is used for the discretization of the central convective flow. To gain further numerical stability implicit overrelaxation omega is set to 1.9. Furthermore, the $2v$ multigrid scheme is applied for both modeling methods. One difference in the numerical setup is the CFL number, its 10 for the pure grid deformation and 0.5 for the combined Chimera method. The Upwind spatial discretization is used for imputation for both types of modeling. Subsequently, the change to the second order central spatial discretization is done, where a convergent solution is obtained for the pure grid deformation by RANS. Due to the large number of gap flows and possible vortex interactions between the leading and trailing edge vortices, a convergent solution for the combined Chimera method cannot be obtained using RANS. Consequently, a switch to URANS is made for this type of modeling. The URANS simulation is performed with a time step of $1/100(c_{ref}/u_\infty)$ and 350 inner iterations. Furthermore, a convergence in the coefficients is

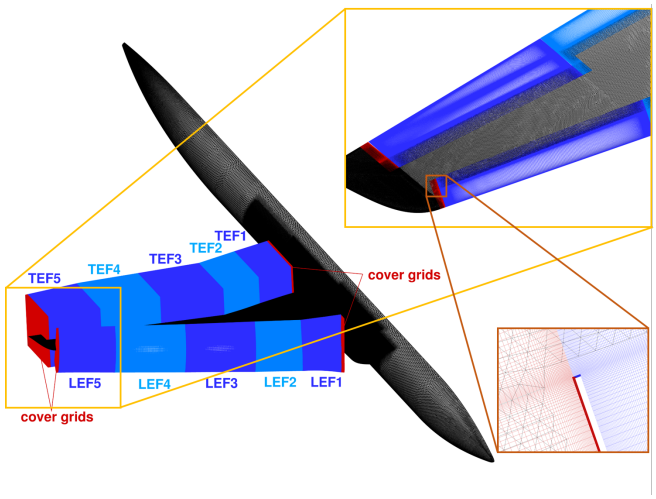

Fig. 1: Representation of the DLR LEISA configuration in the geodetic coordinate system with the Chimera boundary conditions of the individual flap and cover grids. The flap grids are visualized in blue, the cover grids in red.

achieved. In addition, a physical plausible flow field is present, thus the solution can be used for the comparison with the pure grid deformation method. The residuals are a caused of the complex flow case. For the simulations, the compressible flow solver DLR TAU [16] is used. It is a second order hybrid unstructured finite volume CFD code in time and space.

3 Results without Flap Deflection

To analyze the difference between the two flap modeling methods, the distribution of the aerodynamic coefficient over the span as shown in Figure 2(a) is used in the following. The Figure visualizes the spanwise coefficient distribution, showing c_l in blue, c_d in red, and c_m in black. The solid lines correspond to the combined Chimera method, the dashed line to the pure grid deformation. For the evaluation of the spanwise coefficients, 10.000 line in flight sections of the surface solution are analyzed. This number of profile section is necessary to reproduce the gap influence sufficiently well. As shown in Section 2, an overlapping area is needed for the interpolation between two grids. Within the Chimera interpolation region overlapping grids are present on the surface. Hence, a simple integration of local forces and moments would include locally doubled values of c_p and c_f. In order to avoid these doubled values, the baseline grid is not taken into account for the integration in the overlapping region. Due to the unstructured grid type, this method creates a small gap of approximately one element between the control surface grid and the wing surface grid in the postprocessing step. This results in a fluctuation in the spanwise integration of the coefficients for the combined Chimera method. A global difference between the modeling methods can be detected between $\eta = y/0.5b = 0.374$ and $\eta = 0.772$ in the spanwise c_l distribution. Here, the largest difference $|\Delta c_l = 0.0158|$ is obtained at $\eta = 0.515$. Furthermore, a local deviation in the lift coefficient at the transition between TEF4 and TEF5 is visible. Here, the flap depth increases from $15\%c$ to 25%. Thus, a greater influence of the gap is present. First, the c_l drops at the location of the leading edge gap. At the location of the trailing edge gap the c_l increases locally. A more detailed look at the influence of the gap on the c_l is provided by Figure 2(b). Here, the volume streamlines for the TEF at the top as well as for the LEF at the bottom are shown. The flow at the trailing edge gap is divided into four different flow components, which are marked cyan, blue, pink, and gray. Due to the pressure difference between pressure side and suction side, a gap flow occurs from the pressure side to the suction side. The streamlines marked pink and blue form the main part of the gap flow. Due to the fact that the pink vortex region runs along the gap, the blue streamlines do not encounter a sharp edge, thus no vortices are created at the gap side. Consequently, they flow out of the gap interacting with a higher momentum incoming flow above the wing. Accordingly, a tangential component is applied to the flow. As a result the blue streamlines flow around the pink vortex region. In general, the tangential component of the external flow occurs due to the wing sweep. As already discussed, the pink vortex region runs parallel to the outer gap side and is formed at the outflow at the beginning of the gap. Here, the streamlines immediately roll up due to the sharp edge and the interaction with the undisturbed arriving gray marked flow. As a result, the vortex induces a local velocity increase on the wing suction side, causing a local pressure drop and thus an increase in c_l. The last flow component is represented by the cyan colored streamlines. These visualize a separation area in the gap. Due to the sharp edge, the separation area is created by the flow entering the gap from the pressure side at the end wall of the gap. As already described a local c_l reduction is achieved at the LEF gap. To examine this in more detail, Figure 2b (bottom) shows the streamlines at the LEF gap. Here, the flow is divided into four components marked red, blue, green and

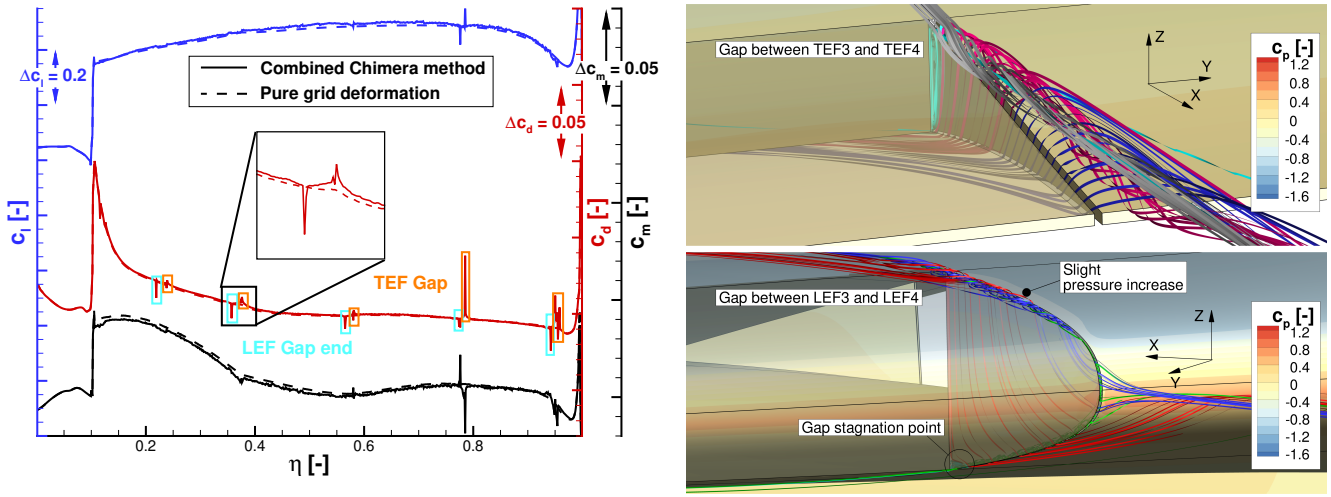

(a) (b)

Fig. 2: Comparison of the flap modeling methods without flap deflection; (a) Spanwise c_l, c_d and c_m distribution of the pure grid deformation (dashed) and combined Chimera method (solid); (b) Representation of the volume streamlines for the TEF gap between TEF3 and TEF4 (top) and the LEF gap between the LEF3 and LEF4 (bottom). The inflow is in positive x direction.

cyan. The green marked streamline enters the gap and immediately undergoes a 90° contour change. This causes a separation that reduces the effective gap width, causing a nozzle effect according to the continuity equation and increases the velocity in this area. As a result, this acceleration causes a horizontal streamline in the separation area. After the separation area, the pressure gradient influences the flow noticeably causing a flow in the direction of the suction side. The global influence of the pressure gradient is visualized by the streamlines marked in blue and red. Both flow components are exiting the gap on the suction side. However, there is a difference between the blue and red marked ones. The blue streamlines already leaves the gap at the leading edge of the wing and interacts with the high momentum flow. Due to the interaction, the flow gains a tangential flow component. This causes the streamlines to undergo a contour change at the junction of the gap and the suction side of the wing, resulting in a vortex region. Subsequently, the blue marked streamlines flow parallel downstream to the LEF gap. In this way, the blue streamlines prevent the red marked from rolling up. In addition, the exiting gap flow and the inflow creates a blockage resulting in a slight pressure increase along the gap, shown in Figure 2b (bottom). Furthermore, a part of the red marked streamlines forms with the cyan ones a stagnation point at the gap end wall. Beginning at the stagnation point, the flow accelerates along the gap end wall towards the wing suction side. This causes a pressure drop leading to an upstream force. In the spanwise c_d distribution no global differences occur between the modeling methods. Only strong local influences of gap realization are visible. The local gap influences have two sources. On the one hand, the described acceleration at the gap end wall results in a drag reduction. On the other hand, an induced drag is generated at the trailing edge gap by the vortex, thus the c_d of the combined Chimera method increases compared to the pure grid deformation. In addition, Figure 2(a) shows that the gap influence on the aileron is significantly stronger due to the higher gap depth. Here, the maximum deviation of $|\Delta c_d = 0.0416|$ is obtained in the TEF gap of the aileron at $\eta = 0.785$. The spanwise c_m distribution shows a slight global difference between the two modeling methods. This starts at the fuselage $\eta = 0.100$ and decreases in the direction of larger span. Locally, at the positions $\eta = 0.237$, $\eta = 0.370$, $\eta = 0.580$, $\eta = 0.780$ as well as $\eta = 0.950$ differences between combined Chimera method and pure grid deformation caused by the gaps. The largest deviation of $|\Delta c_m = 0.0254|$ is obtained at $\eta = 0.780$. In order to estimate the local deviations, the global coefficients are finally compared. Here, a deviation of 1.33% is present for the c_L, and 1.9% for the c_D. Thus, the influence of the gap is mainly local. Thereby, the global c_L of the pure grid deformation is higher compared to the combined Chimera method. In contrast, the global c_D is larger for the combined Chimera method.

4 Results with Flap Deflection

To analyze the influence of the flap deflections on the modeling method, a generic flap deflection of LEF1 = 6°, LEF2=8°, LEF3 =10°, LEF4 =12°, LEF5 = 2.7°, TEF1 = −6.4°, TEF2 = −7.8°, TEF3 = −8.3°, TEF4 = −9°, and TEF5 =−6.2° is investigated. The deflections are based on those for gust load reduction, meaning that sequential flap deflections are present. Figure 3 shows the spanwise distribution of the aerodynamic coefficients. The c_l distribution is given in blue, the c_d in red

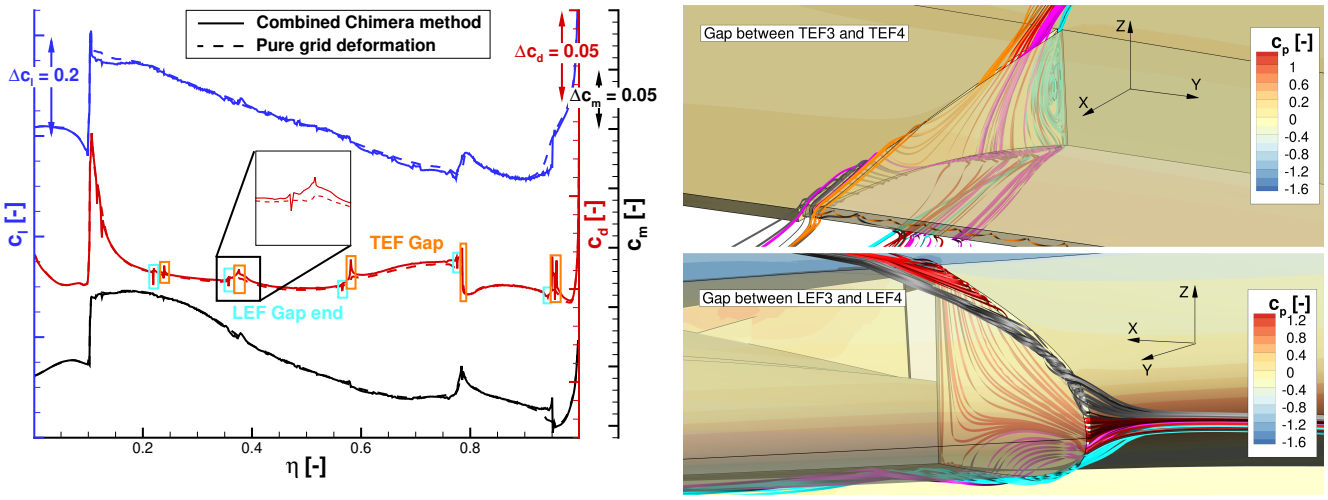

(a) (b)

Fig. 3: Comparison of the flap modeling methods with flap deflection; (a) Spanwise c_l, c_d and c_m distribution of the pure grid deformation (dashed) and combined Chimera method (solid); (b) Representation of the volume streamlines for the TEF gap between TEF3 and TEF4 (top) and the LEF gap between LEF3 and LEF4 (bottom). The inflow is in positive x direction.

and the c_m in black. The solid lines represent the combined Chimera method, the dashed line the pure grid deformation. The c_l distribution shows a local deviation between $\eta = 0.10$ and $\eta = 0.200$. In this range, the pure grid deformation achieves a higher c_l compared to the combined Chimera method. Subsequently, from $\eta = 0.200$ to $\eta = 0.580$, no deviation between the two methods is present. In the region of TEF4, located between $\eta = 0.580$ and $\eta = 0.800$, the difference in the spanwise c_l

increases. Also at the transition from TEF5 to the wing a deviation between the two modeling methods occur. The reason for the deviation is the effective gap enlargement due to the deflection and the resulting pressure exchange between the suction and pressure side. In the spanwise c_d distribution, local differences in the qualitative history between the two modeling methods are evident due to the LEF and TEF gaps. At the LEF gaps the combined Chimera method leads to a c_d reduction. The TEF gaps lead to a c_d increase. Furthermore, at $\eta = 0.380$ as well as $\eta = 0.580$, a strong c_d increase is observed in the combined Chimera method caused by the vortices induced by the LEF deflection. The spanwise c_m distribution does not show any global differences. Only a local deviation is obtained at the transition from TEF5 to the wing. In the spanwise c_m distribution, a qualitative correspondence is present over the entire wing span. Only from $\eta = 0.920$ to $\eta = 0.950$ a deviation occurs. In the corresponding region, the c_l also shows a difference between the two modeling methods. This is due to the blending area between flap and wing in case of the pure grid deformation. The right side of Figure 3 shows the streamlines at the gap between TEF3 and TEF4 at the top and streamlines at the gap between LEF3 and LEF4 at the bottom. In the case of the LEF, the flow field is divided into four components cyan, black, pink and red. The streamlines marked black occur on the wing at the leading edge and flow along the leading edge. Here, due to the downward flap deflection a sharp edge is present. As a result, a vortex is created at the leading edge of the wing and flows downstream along the suction side of the flap and the inner gap side. The vortex causes local velocities at the suction side of the flap as well as at the gap side, resulting in a pressure reduction. Downstream of the LEF, the vorticity decreases due to the interaction with the undisturbed flow. The counterpart to the black marked streamlines are the cyan marked streamlines for the pressure side. A part of them first hits the LEF gap inner side, causing a stagnation at the flap side nose. Consequently, an increased pressure is noticed in this area. In addition, the momentum decreases for this part. The following cyan marked streamlines of higher momentum, push them towards the pressure side, where a vortex is created due to the sharp edge between gap, pressure side, and the high-energy flow. This vortex rolls up over the pressure side of the LEF and causes a pressure reduction due to its locally higher velocity. Subsequently, the vortex flows downstream over the pressure side of the LEF. As described earlier, the cyan marked streamlines, with exception of the stagnation point streamlines, contain a high momentum. Due to this and in combination with the red as well as pink visualized flow components, no flow through the gap exists for the cyan marked component. The red and pink marked flow components run below the cyan marked streamlines. At the side surface of the LEF, both components collide with the gap wall, reducing the momentum contained in the flow. As a result, an increase in pressure occurs on the LEF side. In addition, the reduced momentum makes the flow more sensitive to the pressure gradient across the gap. Consequently, the flow components marked pink as well as red flow through the gap. The red marked component enters at the wing leading edge and flows in the gap to the suction side, where it slightly becomes swirled up. The other gap flow component flows into the gap on the pressure side. The special characteristic here is that the flow does not move to the suction side, instead it flows out on the pressure side. The reason for this is the local pressure reduction caused by the vortex on the pressure side. As a result, the pressure on the pressure side is lower as on the suction side. Thus, a force directed to the pressure side is generated by the pressure gradient.

The flow at the trailing edge is divided into five parts. The cyan marked streamlines forms a separation area at the beginning of the gap. Here, the streamlines run from the suction to the pressure side. The upward deflection of the flap causes a concave contour change on the suction side, decelerating the flow. This results in a local pressure increase. On the pressure side, the deflection causes a convex contour, accelerating the flow and initiating a pressure drop. Consequently, there is a pressure gradient directed towards the pressure side, causing the separation area in the gap to flow in direction of the pressure side. Furthermore, the separation area is significantly larger as the separation area without flap deflection shown in Figure 2(b) (top). The separation area is formed by the flow around the sharp edge at the beginning of the gap. Another flow component is represented by the streamlines marked red and pink. These streamlines also flow from the suction side into the gap, to the pressure side. Downstream, the gradient of the streamlines decreases in the gap. This indicates a lower pressure gradient from the suction to the pressure side. As a result, the orange streamlines flow into the gap from the suction side and return to the suction side. From this point onwards, a resulting pressure gradient from the pressure side to the suction side is present. This is also visible in the black marked streamlines which flow into the gap on the pressure side and out on the suction side. A special characteristic is shown by the pink marked streamlines. These streamlines encounter the red marked on the lower TEF surface. As a result, the pink streamlines can not flow out as normal. Thus, a separation area is created along the pressure side of the trailing edge flap.

The difference in the global coefficients is analyzed last. For the c_{My} the smallest deviation between pure grid deformation and combined Chimera method is obtained with a difference of 0.450%. Here, the value of the combined Chimera method is higher as the value of the pure grid deformation. The largest deviation occurs for the c_{Mx} with 50.4%. Wherein the value of c_{Mx} from the pure grid deformation is higher as the combined Chimera method. However, it has to be considered that it is divided by a small value, which causes the deviation to increase significantly. Furthermore, the deviation in c_L as well as c_D increases by 5.15% and 0.94% to 6.48% and 2.84% compared to the values without flap deflection.

5 Conclusion

The overall aim of this work is the comparison of two modeling methods for the realization of flap deflections. Therefore, the realization of flap deflections using pure grid deformation and the combination of Chimera method are compared without and with a flap deflection. Small deviations in the spanwise coefficient distributions and in the global coefficients between the

two methods are demonstrated. Without flap deflection local qualitative differences are derived in the spanwise c_d distribution by the LEF gap ends as well as by the TEF gap. A relative deviation of 1.90% is generated for the c_D and 1.33% for the c_L. The higher value occurs for c_D for the combined Chimera method. The higher values occurs in pure grid deformation for c_L. Due to the flap deflection, higher deviations between the modeling methods occurs as a result of the generated vortices compared to the case without flap deflection. When the LEF deflects downward, vortices are generated at the LEF that propagates downstream across the wing. This leads to an increase in the induced drag, resulting in local differences between the modeling methods in the spanwise c_d distribution. In the case of the combined Chimera method, the upward TEF deflection has a strong upstream effect. Using the combined Chimera method, the upward deflection increases the effective gap size resulting in pressure compensation. This leads to a lift difference between the modeling methods. Due to these two main gap effects, a difference of 6.48% in c_L results between the modeling methods, while the deviation in c_D is 2.84%. Thus, this work shows a difference in the flow field compared to the pure grid deformation due to the consideration of the spanwise gap. Without flap deflection, the influence of these vortices is almost negligible. Considering flap deflection, a considerable difference between the pure grid deformation and the combined Chimera method occurs. The spanwise distributions with and without flap deflection agree qualitatively well for a wing-fuselage configuration, except for a small number of deviations due to vortex effects. Thus, in this case the application of the grid method is permissible. As a consequence of vortex generation in the flow field, the combined Chimera method should not be neglected for a wing-fuselage configuration and be tested with respect to gust interaction. The same applies for the investigation of the physical flow field due to vortex generation, which is not represented by the modeling via pure grid deformation. The paper at hand demonstrates local differences of the aerodynamic coefficients between the modeling methods for a wing-fuselage configuration. Consequently, the pure grid deformation is a valid method for modeling spanwise segmented flap deflections on a wing-fuselage configuration. With respect to the complexity of grid generation and time effort, the pure grid deformation method is recommended.

Acknowledgements The presented studies are funded by the Federal Ministry for Economic Affairs and Climate Action (BMWi) as part of the LuFo VI-1 project INTELWI ("Aerodynamischer Entwurf und Bewertung dynamischer Steuerflächen für die Reduktion von Böenlasten und Entwicklung einer smarten digitalen Infrastruktur", funding reference: 20A1903B). The authors gratefully acknowledge the support and the computational resources which were provided by the High Performance Computing Center Stuttgart (HLRS). Open access funding enabled and organized by Projekt DEAL.

References

[1] Europäische Kommission und Generaldirektion Mobilität und Verkehr und Generaldirektion Forschung und Innovation, *Flightpath 2050: Europe's vision for aviation : maintaining global leadership and serving society's needs*, Publications Office, 2011.

[2] Schlemmer, C., "Modeling and Simulating the Effects of Different Longitudinal Control Surface Configurations on Flexible Aircraft Flight Dynamics," *Deutscher Luft- und Raumfahrtkongress 2017*, München, September 2017.

[3] European Union Aviation Safety Agency (EASA), *In: Certification Specifications for Large Aeroplane (CS25)*, Amendment 3, EASA, 2007.

[4] Xu, J. and Kroo, I., "Aircraft Design with Active Load Alleviation and Natural Laminar Flow," *Journal of Aircraft*, Vol. 51, No. 5, 2014, pp. 1532–1545.

[5] Krüger, W. R., Dillinger, J., Breuker, R. D., Reyes, M., and Haydn, K., "Adaptive Wing: Investigations of Passive Wing Technologies for Loads Reduction in the CleanSky Smart Fixed Wing Aircraft (SFWA) Project," *Greener Aviation*, Oktober 2016.

[6] Wu, Z., Cao, Y., and Ismail, M., "Gust loads on aircraft," *The Aeronautical Journal*, Vol. 123, No. 1266, 2019, pp. 1216–1274.

[7] Binder, S., Wildschek, A., and De Breuker, R., "The interaction between active aeroelastic control and structural tailoring in aeroservoelastic wing design," *Aerospace Science and Technology*, Vol. 110, 01 2021, pp. 106516.

[8] Miller, E. J., Lokos, W. A., Cruz, J., Crampton, G., Stephens, C. A., Kota, S., Ervin, G. F., and Flick, P. M., "Approach for Structurally Clearing an Adaptive Compliant Trailing Edge Flap for Flight," Tech. rep., National Aeronautics and Space Administration (NASA), September 2015.

[9] Mertins, R., Elsholz, E., Barakat, S., and Colak, B., "3D viscous flow analysis on wing-body-aileron-spoiler configurations," *Aerospace Science and Technology*, Vol. 9, No. 6, 2005, pp. 476–484.

[10] Fillola, G., Carrier, G., and Dor, J.-B., "Experimental Study And Numerical Simulation of Flow Around Wing Control Surface," *ICAS-Secretariat - 25th Congress of the International Council of the Aeronautical Sciences 2006, Hamburg*, Vol. 3, 09 2006.

[11] Reimer, L. and Heinrich, R., "Modeling of Movable Control Surfaces and Atmospheric Effects," *Computational Flight Testing: Results of the Closing Symposium of the German Research Initiative ComFliTe, Braunschweig, Germany, June 11th-12th, 2012*, edited by N. Kroll, R. Radespiel, J. W. Burg, and K. Sørensen, Springer Berlin Heidelberg, Berlin, Heidelberg, 2012, pp. 183–206.

[12] Alcaraz Capsada, L. and Heinrich, R., "Development of the DLR TAU Code for Modelling of Control Surfaces," *Deutscher Luft- und Raumfahrtkongress 2018*, Friedrichshafen, 2019.

[13] Ullah, J., Lutz, T., Klug, L., Radespiel, R., and Wild, J., "Active Gust Load Alleviation by Combined Actuation of Trailing Edge and Leading Edge Flap at Transonic Speeds," *AIAA Scitech 2021 Forum*, Virtual Event, Januar 2021.

[14] Ullah, J., Kamoun, S., Müller, J., and Lutz, T., "Active Gust Load Alleviation by Means of Steady and Dynamic Trailing and Leading Edge Flap Deflections at Transonic Speeds," *AIAA SCITECH 2022 Forum*, San Diego, CA, 2022.

[15] Dargel, G., Hansen, H., und T. Streit, J. W., and und K. Richter, H. R., "Aerodynamische Flügelauslegung mit multifunktionalen Steuerflächen," *Deutscher Luft- und Raumfahrtkongress 2002, Suttgart, 23. - 26. September 2002*, 2002.

[16] Hübner, A.-R. and Reimer, L., "The DLR TAU-code: Recent applications in research and industry." *Eccomas CFD 2006 Conference*, Egmond aan Zee, The Netherlands, 2006.

